Soft Matter

Accepted Manuscript

ROYAL SOCIETY OF CHEMISTRY

www.rsc.org/softmatter

Nonequilibrium phase transitions, fluctuations and correlations in an active contractile polar fluid

Kripa Gowrishankar
Raman Research Institute, Bangalore 560080, India and
Azim Premji University, Bangalore 560100, India

Madan Rao
Raman Research Institute, Bangalore 560080, India and
Simons Centre for the Study of Living Machines, National Centre for Biological Sciences, Bangalore 560065, India
(Dated:)

We study the patterning, fluctuations and correlations of an active polar fluid consisting of contractile polar filaments on a two dimensional substrate, using a hydrodynamic description. The steady states generically consist of arrays of inward pointing asters and show a continuous transition from a moving lamellar phase, a moving aster street to a stationary aster lattice with no net polar order. We next study the effect of a spatio-temporal athermal noise, parametrized by an active temperature T_A, on the stability of the ordered phases. In contrast to its equilibrium counterpart, we find that the active crystal shows true long range order at low T_A. On increasing T_A, the asters dynamically remodel, concomitantly we find novel phase transitions characterized by bond-orientational and polar order upon "heating".

I. INTRODUCTION

A remarkable feature of living cellular systems is that the same ingredients – filaments (actin), motors (myosin) and their regulators, in the presence of ATP – can exhibit an impressive variety of cellular phenotypes [1]. To replicate and quantitatively analyze this spectrum of behaviours in controlled simplified systems, much effort has gone into establishing appropriate in-vitro reconstituted systems [2–5]. Existing in-vitro experiments have dealt with either actin motility assays which exhibit predominantly self-propelled behaviour [2, 3] or systems which are primarily contractile with negligible propulsion [4, 5]. However in-vivo studies [6] have demonstrated that the dynamic interaction of cortical actomyosin with the living cell membrane, results in features where *both* contractility and self-propulsion are simultaneously present. These dual features have been successfully recapitulated in recent reconstitutions of actomyosin thin films on supported membranes [7]. Here we study the nonequilibrium steady states and phase transitions of actively driven collections of filaments-motors in two dimensions using the framework of *active hydrodynamics* or *active gels* [8], which could in principle be used to compare with these experiments [6]. In addition, we conduct a detailed study of the effect of athermal noise in inducing a variety of nonequilibrium phase transitions and build up of spatial correlations in these systems, which can be compared to in-vitro experiments, such as [7].

Our primary experimental motivation stems from recent studies on the nature and dynamics of actin-myosin filaments at the cell cortex and their interaction with membrane components in a variety of cellular systems, such as described in [6, 9, 10]. These studies (and others [11**?** –13]) have shown that in addition to the crosslinked static actin meshwork [14], there is a dynamic population of shorter actin filaments, the former providing a frictional substrate to the dynamics of the latter. These active filaments are regulated by a variety of proteins and undergo both actomyosin contractility, treadmilling and flows.

Our analysis starts with writing dynamical equations for both the concentration and polarization of active filaments, as has been done in many earlier studies [6, 15–18] and reviewed in [8]. Our study primarily explores the regime where the filament concentration is high enough to have orientational order but low enough to have spatial variations of concentration. We study the effects of spatiotemporal active noise that are inevitably present in cellular systems. This not only affects the dynamics in the steady state, but in addition induces novel phase transitions that are characterized by a variety of order parameters and correlation functions. Similar studies on the influence of noise in patterning of active filaments have appeared in [16, 19].

Our work combines both analytical (linear stability analysis) and detailed numerical solutions and complements [16, 20]. Our main results: (a) We find a variety of steady state configurations that include domain walls, lamellar textures, localized inward-pointing asters and spirals; vortices are generically unstable. We first determine and display a robust phase diagram, which includes a transition from a moving aster street phase to a stationary aster lattice phase across a critical line. (b) The 2d active aster lattice phase is stable even in the presence of noise; it shows true long-range order (LRO), in striking contrast to its equilibrium counterpart. (c) Beyond a critical active temperature, this transforms to an aster lattice with quasi long range order (QLRO) during which the localized aster-like configurations remodel with a power law distribution of lifetimes. This phase exhibits strong bond tetratic order. (d) On increasing the active temperature further, we observe a discontinuous transition to a bond nematic phase with an exponen-

tial aster lifetime distribution. Significantly, this bond nematic phase is polar, with power-law orientational correlations [21].

II. DYNAMICS OF ACTIVE FILAMENTS IN TWO DIMENSIONAL CELL CORTEX

The actomyosin system is a collection of permanent force-dipoles, which being polar, induces a net drift of the i^{th} filament relative to the medium, represented by a polarization vector $\mathbf{n}_i$. The hydrodynamic fields are the local concentration $c(\mathbf{r},t)$, polarization density $c(\mathbf{r},t)\mathbf{n}(\mathbf{r},t)$, and hydrodynamic velocity $\mathbf{v}(\mathbf{r},t)$ [22–24].

We will assume that momentum is lost by local friction at the "substrate", thus $\Gamma\mathbf{v} = \nabla\cdot\sigma$, where Γ is the friction coefficient and $\sigma = -Wc\mathbf{nn}$ is the active stress [25] due to the (contractile, $W<0$) force-dipoles. We can use this to eliminate $\mathbf{v}$ from the equations of $\mathbf{n}$ and c, resulting in the well-known active hydrodynamic equations [8], the form of which first appeared in [21],

$$\partial_t\mathbf{n} + \lambda(\mathbf{n}\cdot\nabla)\mathbf{n} = K_1\nabla^2\mathbf{n} + K_2\nabla(\nabla\cdot\mathbf{n}) + \zeta\nabla c + \alpha\mathbf{n} - \beta|\mathbf{n}|^2\mathbf{n} + \mathbf{f} \quad (1)$$

$$\partial_t c = -\nabla\cdot\mathbf{J} = -\nabla\cdot(v_0\,c\,\mathbf{n} - D\nabla c) \quad (2)$$

to lowest order in gradients and fields (contributions from $\mathbf{v}$ appear at higher order). The right side of (1) and (2) represent contributions to active forces/torques and current $\mathbf{J}$.

The parameter $\alpha \approx (\bar{c} - c^*)$ measures the deviation of the mean filament concentration $\bar{c}$ from the Onsager value c^* which fixes the transition to orientational order. K_1 and $K_2 + K_1$ are the non-equilibrium counterparts of bend and splay moduli respectively, and set the orientation relaxation rates of the corresponding distortions. In order to prevent spontaneous distortions, we choose $K_1 > 0$ and $K_2 \geq -K_1$. The terms v_0 and λ are uniquely active in origin, and represent an active advection and a nonlinear active convective contribution, respectively. The athermal noise $\mathbf{f}$ is taken to be white with zero mean and variance equal to T_A/c, where T_A is the active temperature. We have dropped the additive noise term in the c equation, since the multiplicative nonequilibrium driving from the first term in $\mathbf{J}$ is more dominant.

The values of these parameters depend on the microscopic active processes controlling actin dynamics. In a cellular context, several microscopic active processes, such as treadmilling and actomyosin contractility, occur simultaneously. We therefore independently vary the parameters entering (1) and (2). For the contractile motor-filament system, $\zeta v_0 > 0$, which is *opposite* to the flocking case considered in [21]. Below we provide a quick rationale for this.

One way to see this is based on suspension hydrodynamics [26] namely, $md\mathbf{U}/dt = \nabla\cdot\sigma$, where $\mathbf{U}$ is the particle velocity and σ is the particle stress. For an active polar particle, we identify the former with the polarization, $\mathbf{U} = v_0\mathbf{n}$, and the latter with the active stress $\sigma = -Wc\mathbf{nn}$, with $W<0$ for contractile stresses. This immediately leads to the $\zeta\nabla c$ term in the $\mathbf{n}$-equation and the condition that $\zeta v_0 > 0$ for contractile flows - a kind of negative pressure.

A second way is to realise that there are in fact three nonlinear active convection terms, $\lambda_1(\mathbf{n}\cdot\nabla)\mathbf{n}$, $\lambda_2\nabla|\mathbf{n}|^2$ and $\lambda_3\,\mathbf{n}(\nabla\cdot\mathbf{n})$ [21] - of which we have kept only the first one in (1), on the grounds that it is the most relevant in 2d [21]. Since there is no restriction on the sign of λ_2, we note that by including the term $\nabla|\mathbf{n}|^2$ and recognising that $|\mathbf{n}|^2 \propto c$, we are immediately lead to the $\zeta\nabla c$ term, with an effective $\zeta > 0$ [18].

Finally, we indicate two rather direct ways of arriving at this form of the 'pressure' term [27, 28]. One involves including a density dependent motility in a collection of active polar rods with an explicit alignment interaction [27]; the continuum hydrodynamic equations derived from this contains a pressure term whose sign can be reversed when the motility is made dependent on the local density. The other involves writing down separate dynamical equations for the bound myosin density and the polar actin filament density [28]; upon integrating out the myosin density field, we arrive at effective equations for active polar filaments, with an effective "negative pressure term"

Note that though we refer to this feature as arising from contractility, it is strictly different from the usual sense in which contractility is used, as a *fluid* (described by a hydrodynamic velocity) subject to contractile force dipoles characterized by $W<0$ in the active stress.

It is instructive to illustrate the parameters' typical microscopic origins : (a) High and positive values of K_1, K_2, α and λ favour ordered bundles of filaments and hence depend on the effect of bundling proteins, such as fascin, as in [2]; (b) ζ measures the re-orientation rate of filaments along concentration gradients, and hence overcomes the effect of bundling proteins to form defects such as asters, spirals and walls. We will see shortly that these defects are stabilized precisely when $\zeta v_0 > 0$. Both ζ and v_0 hence depend on concentrations and stepping rates of myosin motors.

With these parameters, one can construct the following independent length scales – (i) correlation lengths L_c, given by $\sqrt{K_1/\alpha}$ and $\sqrt{(K_1+K_2)/\alpha}$, (ii) extrapolation lengths L_e [29], given by K_1/ζ and $(K_1+K_2)/\zeta$ and (iii) Péclet length, $L_p = D/v_0$, the ratio of diffusion coefficient to advection. We will predominantly work in the regime where both L_c and L_e are small, further, we study the phase diagram when the magnitude of λ is zero or small.

III. LINEAR STABILITY, STEADY STATE PHASE DIAGRAM AND LOCALIZED DEFECTS

We first explore the phase diagram when the active temperature, $T_A = 0$, by analysing the stability of two possible steady states: (i) uniform orientationally dis-

ordered ($c(\mathbf{r},t) = 1, \mathbf{n}(\mathbf{r},t) = 0$) and (ii) uniform orientationally ordered ($c(\mathbf{r},t) = 1, \mathbf{n}(\mathbf{r},t) = \hat{\mathbf{x}}$). (Henceforth c and $\mathbf{n}$ are measured in units of the mean filament concentration $\bar{c}$ and $\sqrt{\alpha/\beta}$). This is done by adding perturbations $(\delta c(\mathbf{r},t), \delta\mathbf{n}(\mathbf{r},t))$ to $(c(\mathbf{r},t), \mathbf{n}(\mathbf{r},t))$ for the two cases, and truncating the resultant equations of motion to retain all terms upto linear order in the perturbations. We then expand the perturbations in terms of their fourier modes $\delta c(\mathbf{k},t) = \int_{\mathbf{r}} \delta c(\mathbf{r},t) e^{i\mathbf{k}\cdot\mathbf{r}}$ and $\delta\mathbf{n}(\mathbf{k},t) = \int_{\mathbf{r}} \delta\mathbf{n}(\mathbf{r},t) e^{i\mathbf{k}\cdot\mathbf{r}}$.

The resulting linearized dynamical equations are of the form,

$$\partial_t \begin{bmatrix} \delta c(\mathbf{k},t) \\ \delta n_x(\mathbf{k},t) \\ \delta n_y(\mathbf{k},t) \end{bmatrix} = \mathbf{A} \begin{bmatrix} \delta c(\mathbf{k},t) \\ \delta n_x(\mathbf{k},t) \\ \delta n_y(\mathbf{k},t) \end{bmatrix}$$

where $\mathbf{A}$ is a 3×3 matrix, the eigenvalues of $\mathbf{A}$ indicating the stability of the corresponding perturbations.

For case (i), the uniform orientationally disordered phase, $\mathbf{A}$ has the form

$$\mathbf{A} = \begin{bmatrix} -Dk^2 & -iv_0k_x & -iv_0k_y \\ i\zeta k_x & -K_1k^2 - K_2k_x^2 + \alpha & -K_2k_xk_y \\ i\zeta k_y & -K_2k_xk_y & -K_1k^2 - K_2k_y^2 + \alpha \end{bmatrix}.$$

This phase is always unstable when $\alpha > 0$, and the magnitude of $|\mathbf{n}|$ grows and saturates at $|\mathbf{n}| = 1$. When $\alpha < 0$, this phase is stable unless ζ crosses a critical threshold $\zeta = -D\alpha/v_0$. One of the eigenvalues of $\mathbf{A}$, which gives the growth rate of modes of wavenumber k, becomes positive beyond this threshold, and is given by

$$\omega \approx -k^2\left(D + \frac{\zeta v_0}{\alpha}\right) + k^4\frac{\zeta v_0}{\alpha^3}\left[\alpha\left(D - (K_1+K_2)\right) + \zeta v_0\right].$$

The growth corresponds to a clumping instability, whose scale is set by the inverse of the maximal unstable mode $k_d = \sqrt{\delta/K_1D}$, where $\delta = \zeta v_0 + D\alpha$.

For case (ii), the uniform orientationally ordered phase, $\mathbf{A}$ has the form

$$\begin{bmatrix} -Dk^2 - iv_0k_x & -iv_0k_x & -iv_0k_y \\ i\zeta k_x & -K_1k^2 - K_2k_x^2 - 2\alpha & -K_2k_xk_y \\ i\zeta k_y & -K_2k_xk_y & -K_1k^2 - K_2k_y^2 \end{bmatrix}$$

This phase is stable when $\alpha > 0$ and $\zeta = 0$ and becomes spontaneously unstable to splay distortions as soon as $\zeta v_0 > 0$. Splay distortions of wavenumber k_y grow with a rate,

$$\omega \approx k_y\sqrt{\zeta v_0} - k_y^2(D + K_1 + K_2). \tag{3}$$

Taking the ordering direction to be along $\hat{\mathbf{x}}$, we find that there is a band of unstable wavevectors centered around

$$k_x = 0,$$
$$k_y \equiv k_0 = \frac{\sqrt{\zeta v_0}}{(D + K_1 + K_2)}. \tag{4}$$

The final steady state configurations when α and ζ are positive, depend on the extrapolation length L_e relative to the other lengths, and can be obtained by numerically solving (1) and (2) in dimensionless form, choosing the units of length and time to be $D/2.5v_0$ and $D/2.5v_0^2$ respectively. Values of other parameters are written in these units. We choose a large value of α and β, such that the magnitude of $\mathbf{n}$ in the ordered phase is close to unity almost everywhere. Beyond this, their exact values are irrelevant, as we have checked. Parameter values appropriate to the in-vivo context described in the Introduction, have been described in [6]. We use an implicit *alternate direction operator splitting* scheme with length and time discretizations chosen to be $\Delta x = 1$ and $\Delta t = 0.01$ respectively [30], with initial conditions for $c(\mathbf{r},\mathbf{t})$ and $\mathbf{n}(\mathbf{r},\mathbf{t})$ being homogeneous and random. The boundary conditions are chosen to be periodic; however, our results hold for other boundary conditions as well, as long as the system size $L \gg L_c$. In order to maintain conservation and non-negativity of the local concentration, we use symmetric spatial derivatives (that add up to zero over the whole system) with an adaptive grid size Δt.

Since $\zeta v_0 > 0$, the steady state configurations generically consist of a collection of finite-size defects such as inward-pointing asters [31, 32], inward-pointing spirals or walls. This might be expected, since the filament current $\mathbf{J} \propto \mathbf{n}$ and the steady state equations for $\mathbf{n}$ is roughly a vector Poisson equation with $\frac{\zeta}{K_1}\nabla c$ as source.

We have explored the small extrapolation length regime in some detail, where upon increasing ζ, we encounter the following phases (Fig.1) : (i) *Lamellar texture* - consisting of alternate stripes of filaments oriented along $\hat{\mathbf{x}}$ separated by a scale $1/k_0$. (ii) *Aster street* - consisting of alternate stripes of filaments oriented along $\hat{\mathbf{x}}$ and inward-pointing asters with scale $1/k_0$ and an aster size given by L_p, the Péclet length. and (iii) *Aster lattice* - consisting of a square lattice of inward-pointing asters where the aster size is again L_p and the 'lattice spacing' is $1/k_0$ ($\geq L_p$). A similar kind of square lattice configuration and stability have been described in [15].

To see why asters should settle into a square lattice, note that in the limit $\lambda = 0$, the right side of (1) can be written as a derivative of a 'energy-functional' (strictly a lyapunov functional), thus steady state solutions are minimisers of this 'energy' – we find that the 'energy density' of asters (in units of K_1) arranged in a square ($E_{sq} = -35$) is lower than in a triangular ($E_{tr} = -29$) unit cell. As a check, we have verified that this square lattice persists when we reduce the spatial discretization to be much smaller than the aster lattice spacing.

Since $\langle\mathbf{n}\rangle \neq 0$ implies a movement of the active filaments with respect to the medium, the lamellar texture and aster street are moving phases, while the aster lattice is a stationary phase. The mean drift velocity given by $|\langle c\mathbf{n}\rangle|$ shows a discontinuous jump across the lamellar-aster street transition and a continuous transition at the

street-lattice phase boundary (Fig.2), where we find

$$|\langle c\mathbf{n}\rangle| \sim |\zeta - \zeta_c|^{\gamma}\,, \tag{5}$$

with $\gamma \approx 1.38 \pm 0.05$. While we do not have an analytic explanation for the exponent value, it is easy to see why $\gamma > 1$ – as one approaches the aster lattice phase from the street side, the filaments are drawn into the asters from the nearby parallel filaments by the $\zeta\nabla c$ term, as a result of which there is a nonlinear positive feedback which draws in filaments more strongly, enhancing the rate at which the net drift velocity vanishes.

When we ignore density variations (as was done in [23]), the nature of defects and their size is strictly set by boundary conditions. This could be argued to be acceptable when the active filaments are long and rigid or when their concentration is so high that steric considerations do not allow for density variations. However, as discussed in the Introduction, here we are interested in a regime where the density is high enough so as to have orientational order but low enough to have significant density variations. The effects of including variations in concentration is that (a) only the inward-pointing aster defects are stable and (b) the defects are localized and have a finite size set by the internal dynamics (i.e., they are insensitive to the boundary for large enough system sizes, unlike in [23]).

To see why other defect configurations such as vortices or outward-pointing asters reported in [23] are unstable when we include the dynamics of the concentration field, we study the linear instability of these defects to radial fluctuations. We begin by parametrizing a vortex by $\mathbf{n}_0(\mathbf{r}) = \hat{\mathbf{e}}_\theta$, $c_0(\mathbf{r}) = c_0$. Away from the core of the vortex, the magnitude of the polarization vector is nearly 1. For ease of calculation, we change variables from $c(\mathbf{r})$ to $u(\mathbf{r}) = dc(\mathbf{r})/dr$. Consider the perturbation, $\mathbf{n}(\mathbf{r}) = \mathbf{n}_0 + \delta n \hat{\mathbf{e}}_r$, and $u(\mathbf{r}) = u_0 + \delta u$, where the perturbations $\delta n(t), \delta u(t)$ are independent of $\mathbf{r}$. Equations (1), (2) to linear order in perturbations are given by,

$$\partial_t \delta n = -\frac{K + \delta K}{r^2}\delta n + \zeta\, \delta u \tag{6}$$

$$\partial_t \delta u = \frac{v_0 c_0}{r^2}\delta n - \frac{D}{r^2}\delta u \tag{7}$$

Clearly the perturbations about the vortex grow at a rate $\sim \sqrt{c_0 v_0 \zeta}/r$ where r is the distance from the core. For a vortex of finite-size R, we set $r = R$ to obtain the the growth rate of the instability. The vortex is seen to evolve into an inward-pointing spiral or an aster.

Allowing for significant concentration variation also generates defects of finite size and independent of boundary conditions as long as system sizes are large. For large enough ζ, finite-size defects are generated by the internal dynamics, a balance between $K\nabla^2\mathbf{n}$ and $\zeta\nabla c$, and a balance between inward (active) advective flux $v_0 c\mathbf{n}$ and diffusive flux $D\nabla c$ and is *insensitive* to the boundary for large systems. This gives rise to stable localized defects of inward pointing asters, whose size is set by the Péclet length D/v_0. Consequently all domain sizes including elliptical domains referred to in this paragraph are set by D/v_0. The scale $1/k_0$, obtained from a linear stability analysis, refers to the distance between asters. Note that when advection is negligible, the defect size is set by the ratio of the spontaneous splay coupling strength ζ to a Frank modulus, K, as it would be in an equilibrium polar liquid crystal [29].

It is possible to obtain the other defect configurations, especially the inward spiral asters, when the bend and splay distortions are comparable or even when the values of λ are large. Being active such spiral asters would rotate with an angular velocity [23]. On the other hand, to realize stable vortex configurations, one would need to include the binding to cross-linking proteins. It would be interesting to study the active analogue of the phase diagram of achiral tilt textures in a circular domain at equilibrium [33, 34]. In a different regime, when the extrapolation length L_e is large, one obtains transient configurations of moving walls with filaments oriented normal to it. This resembles the configurations seen in reconstitution experiments [2, 3] and numerical simulations [20].

IV. EFFECT OF ACTIVE NOISE : FLUCTUATIONS, CORRELATIONS AND NEW PHASES

We now study the effects of active stochasticity on the steady state actin patterns by numerical integration of Eqs. (1),(2) with noise, whose strength is parametrized by the active temperature, $T_A > 0$. At high ζ, where the steady state is an aster (square) lattice at $T_A = 0$, low noise results in phonon vibrations of the aster lattice. To quantify the state at low T_A, we compute the structure factor $S(\mathbf{q})$ from the fluctuations of the density of asters, which we define as

$$\rho_{ast}(\mathbf{r}) = -c(\mathbf{r})\nabla\cdot\mathbf{n}(\mathbf{r}) \tag{8}$$

(since asters correspond to large negative values of divergence of $\mathbf{n}$).

The structure factor shows Bragg peaks indexed by the reciprocal lattice vectors of a square, the amplitude of the peaks scales as L^2 for $0 < T_A < T_A^*$ (Fig.3) - unlike the 2d equilibrium solid, the 2d active solid shows true long range order (LRO) at non-zero T_A ! Beyond T_A^*, the amplitude of the Bragg peaks scales as $L^{2-\eta(T_A)}$, suggesting a transition to a solid with quasi-long range order (QLRO). We confirm this from a scaling plot of the structure factor $S(q)$ versus $qL^{2-\eta}$ for $q \parallel \mathbf{G}$, the reciprocal lattice vector $\mathbf{G} = [1, 1]$ (Fig.3). This result should come as a surprise, since, as we remind the reader, this is an active stabilization of *positional* LRO and not orientational LRO, as discussed in [21].

In addition we compute bond-orientational order parameters, namely tetratic $\Psi_4 \equiv \langle e^{i4\theta}\rangle$ and nematic $\Psi_2 \equiv \langle e^{i2\theta}\rangle$, where θ is the orientation of the bonds between

nearest neighbour asters and the $\hat{\mathbf{x}}$-axis. Further increase in the active temperature T_A, results in an elaborate phase diagram in the $\zeta - T_A$ plane (Fig.4). As seen in Fig.5, the bond orientational order parameters Ψ_4 and Ψ_2 clearly indicates a discontinuous transition from a QLRO solid with tetratic order to a bond-nematic liquid. This jump in the order parameter Ψ_2 decreases on decreasing ζ and approaches zero at a multicritical point.

These structural transitions driven by the activity temperature T_A (Fig.4), are associated with a remodeling of the asters; beyond the active solid phase the asters break and reappear transiently, resulting in a decrease in the mean aster density with increasing T_A [6]. The distribution of lifetimes of the asters is a power-law in the tetratic phase ($P(\tau) \sim \tau^{-2.7}$) and exponential in the nematic phase [6]. Interestingly, the decrease in the number density of asters is accompanied by an increase in the net polarization $\langle c\mathbf{n}\rangle$ which jumps from being zero in the solid to a nonzero value in the tetratic and nematic phases (Fig.6). Thus the effect of the active noise is to increase the polar order, weaning away filaments from the asters (order by "heating"). Simultaneously, we find that orientational fluctuations about the ordered direction are massless. Figure 6 shows a power-law fit to the (unconnected) correlation function $C(\mathbf{q}) \equiv \langle \mathbf{n}(\mathbf{q},t) \cdot \mathbf{n}(-\mathbf{q},t)\rangle$ versus $q_\perp$ (wave-vector perpendicular to the ordering direction, taken to be along $\hat{\mathbf{x}}$; deviations occur both at low $q_\perp$ (corresponding to system size L) and high (corresponding to distance between asters, which decreases with increasing ζ). From a finite size analysis, we find that $C(\mathbf{q}) \sim |q_\perp|^{-\theta}$, with $\theta = 1.8 \pm 0.031$. With a further increase in T_A, the system eventually settles into an orientationally disordered phase.

The sequence of transitions described above was in the high ζ regime. At lower values of ζ, when the zero temperature phase is an aster street, an increase in T_A drives the steady state directly into a bond nematic phase. Decreasing ζ further, i.e., starting from the lamellar texture phase, we find that an increase in T_A leads to elliptical domains of whose scale is set by the correlation length, L_c and D/v_0. In fact, even when $\zeta \leq 0$ and small, a nonzero T_A produces these elliptical domains, as a consequence of the advection current v_0.

V. DISCUSSION

To conclude, we have made a detailed study of the nonequilibrium phases and transitions of active filaments in two dimensions, both with and without active noise. The collective behaviour of active filaments gives rise to a variety of defect phases, which should be experimentally observable.

There are several directions for the future, of which we list a few : (i) The phase diagram, Fig.1, while fairly rich, still leaves out the parameter regime corresponding to high values of λ [18]. (ii) The evidence for the stability of the active crystal in 2d is purely based on our numerics - one would like to understand this from a more theoretical basis by formulating a hydrodynamic theory of a polar active solid. (iii) In the presence of inhomogeneous contractility (i.e., when parameters such as ζ are spatially inhomogeneous), we find that the aster coalesce. Within the calculation presented, the scale of the asters is set by the ratio D/v_0, though simple extensions of Eqs. (1),(2) to include higher order terms or other processes can lead to an increase in the aster scale. One simple way is to increase the local concentration of filaments so as to attain a jammed aster configuration due to steric hinderance. Indeed the same result can be obtained with a lower concentration of filaments with the help of crosslinkers. An interesting alternative is to have a higher depolymerization rate k_d at the aster cores balanced by a polymerization at the periphery. This would make the core size and hence the aster size bigger. A dramatic example of this phenomena is in the immunological synapse, where large actin asters, of order several microns, drives the clustering of T-cell receptors [10].

VI. ACKNOWLEDGMENTS

We thank S. Mayor, S. Ghosh, S. Saha, K. Husain, P. Srivastava, S. Ramaswamy and S. Sengupta for discussions and support.

[1] E.S. Chabbra and H.N. Higgs, *Nat. Cell Biol.*, 2007, **9**, 1110.
[2] V. Schaller, C. Weber, C. Semmrich, E. Frey and A.R. Bausch, 2010, *Nature* **467**, 73.
[3] T. Butt, T. Mufti, A. Humayun, P.B. Rosenthal, S. Khan and Molloy J, *J. Biol. Chem.*, 2010, **285**, 4964.
[4] F. Backouche, L. Haviv, D. Groswasser and A. Bernheim-Groswasser, *Phys. Biol.*, 2006, **3**, 264.
[5] D. Smith, F. Ziebert, D. Humphrey, C. Duggan, M. Steinbeck, W. Zimmerman and J. Kas, *Biophys. J.*, 2007, **93**, 4445.
[6] K. Gowrishankar, S. Ghosh, S. Saha, C. Rumamol, S. Mayor and M. Rao, *Cell*, 2012, **149**, 1353.
[7] D. V. Köster, K. Husain, E. Iljazi, P. Bieling, D. Mullins, M. Rao and S. Mayor, *u*nder review.
[8] M.C. Marchetti, J.F. Joanny, S. Ramaswamy, T.B. Liverpool, J. Prost, M. Rao and R.A. Simha, *R*ev. Mod. Phys., 2013, **85**, 1143.
[9] T.S. Van Zanten, A. Cambi, M. Koopman, B. Joosten, C.G. Figdor and M.F. Garcia-Parajo, *Proc. Natl. Acad. Sci.*, 2009, **106**, 18557 (2009).
[10] Y. Kaizuka, A.D. Douglass, R. Varma, M.L. Dustin and R. Vale, *Proc. Nat. Acad. Sc.*, 2007, **104**, 20296.

[11] M.L. Cano, D. Lauffenburger and S.H. Zigmond, *J. Cell Biol.*, 1991, **115**, 677-687.
[12] E.M. Reichl, Y. Ren, M.K. Morphew, M. Delannoy, J.C. Effler, K.D. Girard, S. Divi, P. Iglesias, S.C. Kuo and D.N. Robinson, *Curr. Biol.*, 2008, **18**, 471-480.
[13] Collins et al., *Curr. Biol.*, 2011, **21**, 1167-1175.
[14] N. Morone, T. Fujiwara, K. Murase, R.S. Kasai, H. Ike, S. Yuasa, J. Usukura and A. Kusumi, *J. Cell Biol.*, 2006, **174**, 851.
[15] F. Zeibert and W. Zimmerman, *Eur. Phys. J.* E, 2005, **18**, 41.
[16] I.S. Aronson and L.S. Tsimring, *Phys. Rev. E*, 2005, **71**, 050901(R); *Phys. Rev. E*, 2006, **74**, 031915.
[17] K. Kruse and K. Doubrovinski, *Eur. Phys. Lett*, 2008, **83**, 18003.
[18] A. Gopinath, M. F. Hagan, M. C. Marchetti and A. Baskaran, *Phys. Rev. E*, 2012, **85**, 061903.
[19] S. Swaminathan, F. Ziebert, I.S. Aranson and D. Karpeev, *Euro. Phys. Lett.*, 2010, **90**, 28001.
[20] S. Mishra, A. Baskaran and M.C. Marchetti, *Phys. Rev. E*, 2010, **81**, 061916.
[21] J. Toner and Y. Tu, *Phys. Rev. Lett.*, 1995, **75**, 4326; *Phys. Rev. E*, 1998, **58**, 4828.
[22] R.A. Simha and S. Ramaswamy, *Phys. Rev. Lett.*, 2002, **89**, 058101.
[23] K. Kruse, J.F. Joanny, F. Julicher, J. Prost and K. Sekimoto, *Phys. Rev. Lett.* 2004, **92**, 078101.
[24] T.B. Liverpool and M.C. Marchetti, *Phys. Rev. Lett.*, 2003, **90**, 138102.
[25] Y. Hatwalne, S. Ramaswamy, M. Rao and R.A. Simha, *Phys. Rev. Lett.*, 2004, **92**, 118101.
[26] D.R. Foss and J.F. Brady, *J. Fluid Mech.*, 2000, **407**, 167.
[27] F. D. C. Farrell, M. C. Marchetti, D. Marenduzzo and J. Tailleur, *Phys. Rev. Lett.*, 2012, **108**, 248101.
[28] K. Husain and M. Rao, *in preparation.*
[29] P.G. deGennes and J. Prost, *The Physics of Liquid Crystals*, 1993, Clarendon Press.
[30] W. Press, S. Teukolsky, W. Vetterling and B. Flannery, *Numerical Recipes*, 1992, Cambridge University Press.
[31] H.Y. Lee and M. Kardar, *Phys. Rev. E*, 2001, **64**, 056113.
[32] S. Sankararaman, G.I. Menon and P.B. Sunil Kumar, *Phys. Rev. E*, 2004, **70**, 031905.
[33] D. Pettey and T.C. Lubensky, *Phys. Rev. E*, 1999, **59**, 1834.
[34] R.C. Sarasij and M. Rao, *Phys. Rev. Lett.*, 2002, **88**, 088101; R.C. Sarasij, P. Srivastava and M. Rao, *Phys. Rev. E*, 2012, **85**, 041920.

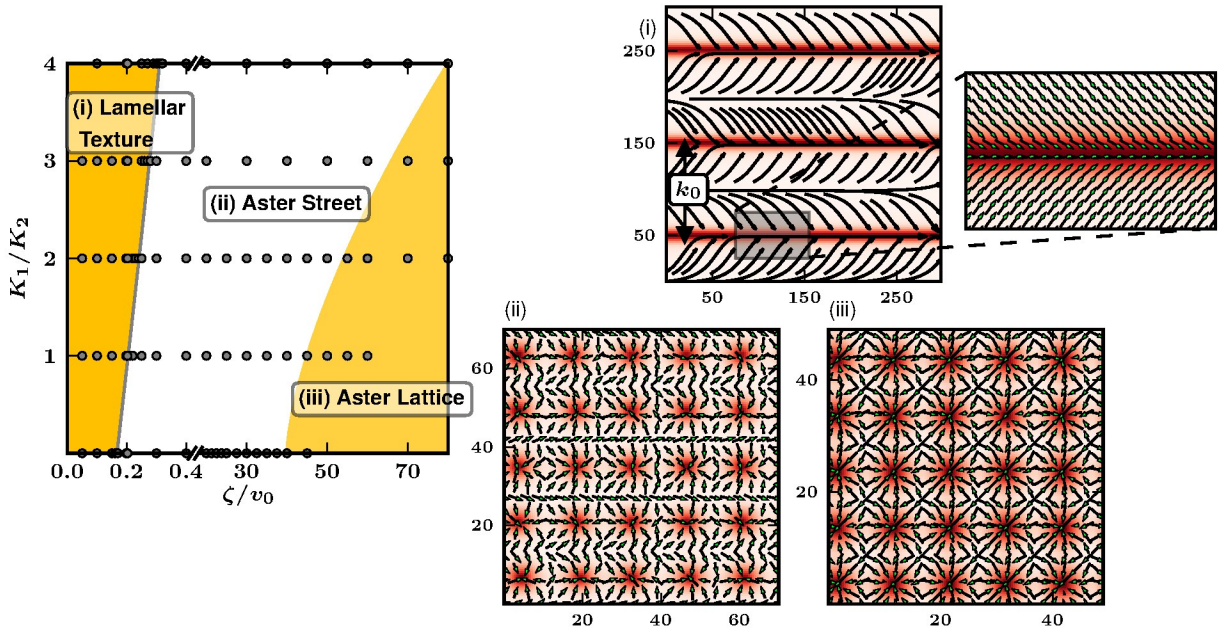

FIG. 1. (a) Phase diagram in K_2/K_1 versus ζ/v_0 at $T_A = 0$, where $D = 2.5$, $\alpha = \beta = 100$ and $L = 100$ in dimensionless units (see text), shows 3 phases - (i) Lamellar texture (ii) Aster street and (iii) Aster lattice. Representative configurations of c (shading) and $\mathbf{n}$ (streamlines in (i) and arrows in (ii) and (iii)), when $K_1 = 2.5$, $K_2 = 0$, $v_0 = 1$, and $\zeta = 0.1$ (i), 5 (ii) and 80 (iii), shown alongside. (i) and (ii) are *moving* phases, (iii) is a globally stationary phase.

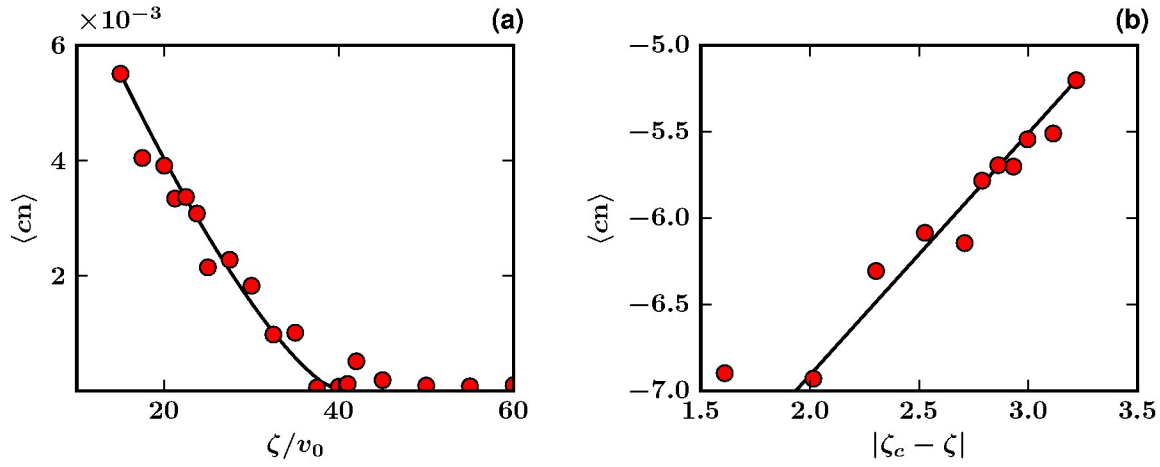

FIG. 2. (a) Net polarization $\langle c\mathbf{n} \rangle$ goes to zero, as the parameter ζ/v_0 changes across the moving to stationary phases, with a power law behaviour $\langle c\mathbf{n} \rangle \sim |\zeta - \zeta_c|^\gamma$, where $\zeta_c = 40$ and $\gamma \approx 1.4$ (b) is a log-plot (base e), lines show fit.

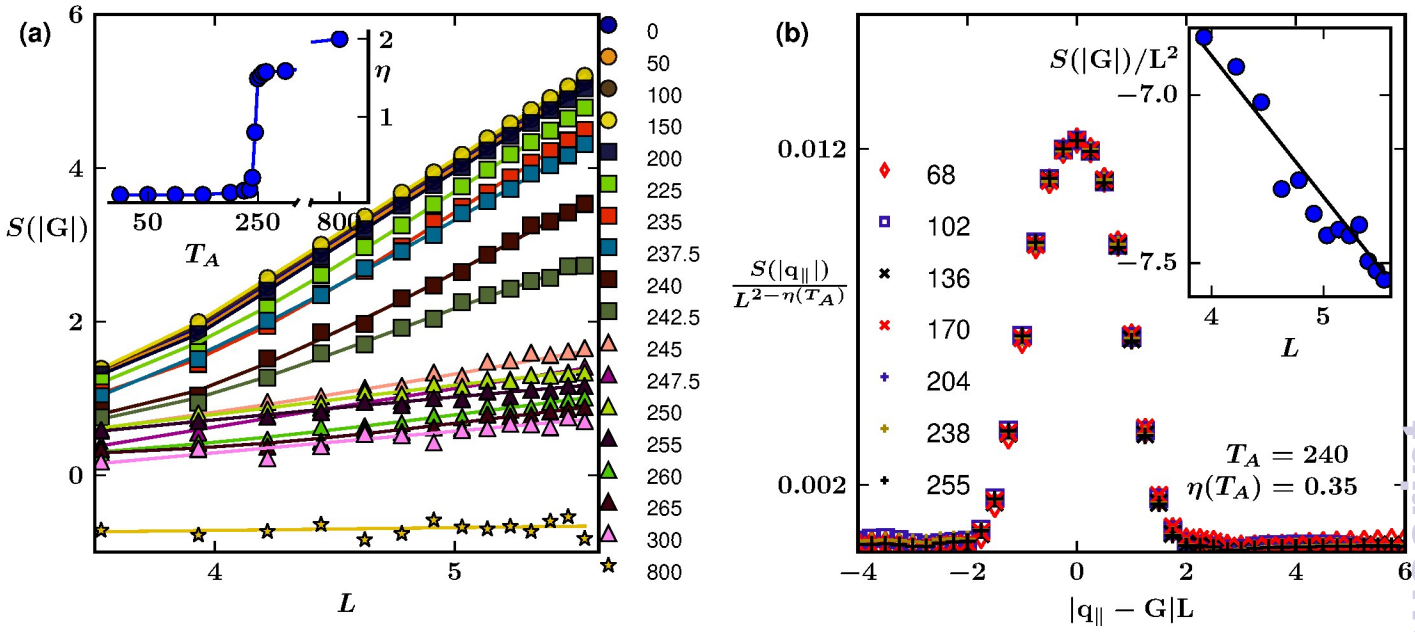

FIG. 3. (a) Log-plot (base e) of the peak amplitude of the aster-density structure factor S evaluated at the reciprocal lattice vector $\mathbf{G}$ of the square, as a function of system size L, over a range of T_A (symbols to the right). For $0 < T_A < 160$, $S(|\mathbf{G}|) \propto L^2$, implying true LRO. Beyond this temperature, $S(|\mathbf{G}|) \propto L^{2-\eta(T_A)}$, where $\eta(T_A)$ (inset) suggests a transition to QLRO. At higher T_A, there is a transition to short range order (SRO). (b) At $T_A = 240$ (QLRO phase), S evaluated about the peak ($q_\parallel$ is parallel to $\mathbf{G}$) exhibits a finite-size scaling form (symbols denote different L). Inset shows a log-plot (base e) of the scaling of the peak amplitude of S with L at fixed η. Here, $\zeta = 100$, other parameters same as Fig. 1.

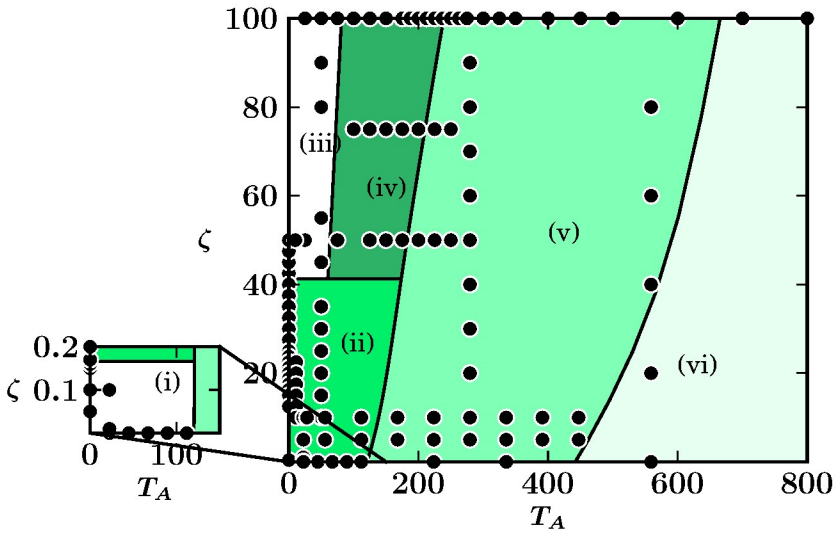

FIG. 4. (a) ζ-T_A phase diagram : (i) Lamellar texture (ii) Aster street (iii) Aster lattice (iv) Bond tetratic (v) Bond nematic and (vi) Isotropic phases. Other parameters same as Fig. 1.

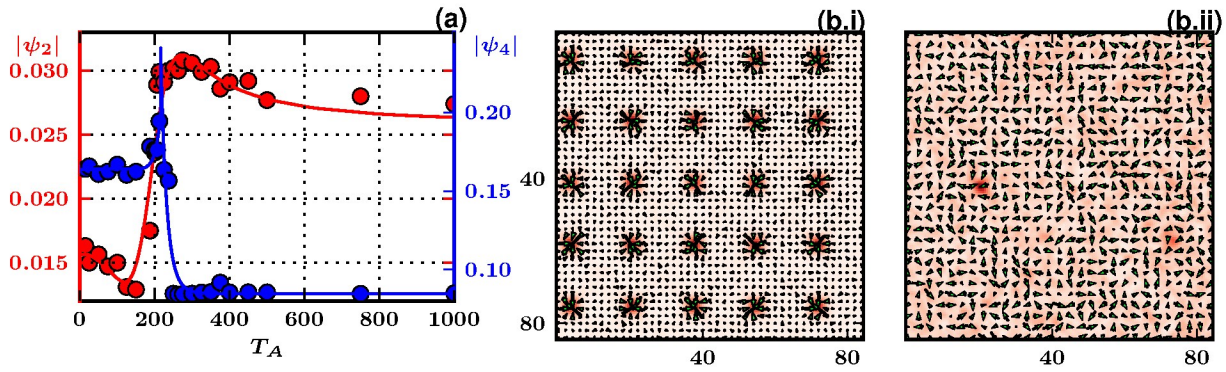

FIG. 5. (a) Bond orientational order parameters $|\Psi_2|$ (*nematic*, red) and $|\Psi_4|$ (*tetratic*, blue) versus T_A across the (iv) $\rightarrow$ (v) transition, with $\zeta = 100$. (b) Typical snapshot of spatial configuration of (i) bond-tetratic and (i) bond-nematic phases. Arrows indicate local orientation of $\mathbf{n}$. Rest of parameters as in Fig. 1.

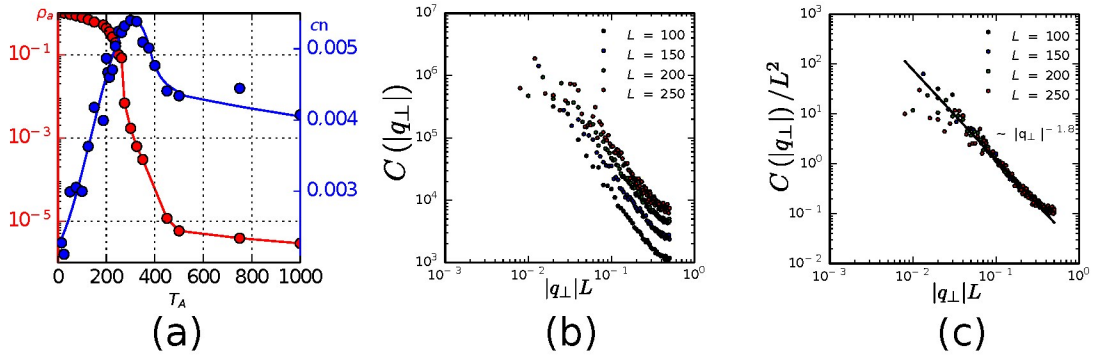

FIG. 6. (a) Sharp drop in filament density within asters ρ_a (log-plot) with T_A (blue) and the corresponding variation of the order parameter $c\mathbf{n}$ (red), with parameter values same as Fig. 3. (b) Log-plot (base 10) of $C(\mathbf{q}) \equiv \langle \mathbf{n}(\mathbf{q},t) \cdot \mathbf{n}(-\mathbf{q},t) \rangle$ vs $|q_\perp|L$ for bond nematic phase (circles) at different system sizes L. The power law regime lies between the lower wavevector cutoff due to L and upper wavevector cutoff due to inter-aster distance. (c) Finite-size scaling collapse of the data shows a power law fit to $C(\mathbf{q}) \sim q^{-\theta}$ with $\theta = 1.8 \pm 0.031$ (black solid line). Parameters $\zeta = 10$, $T_A = 100$, rest same as Fig. 1.